



# 3D Paleoseismology of the Dog Valley Fault (California, USA) from iOS Lidar and Structure-from-Motion Photogrammetry

Ian K.D. Pierce  <sup>\*1,2</sup>, Richard Koehler  <sup>1</sup>

<sup>1</sup>Nevada Bureau of Mines and Geology, University of Nevada, Reno, USA, <sup>2</sup>Department of Earth Sciences, University of Oxford, Oxford, UK

**Author contributions:** *Conceptualization:* I. Pierce, R. Koehler. *Data Curation:* I. Pierce. *Formal Analysis:* I. Pierce, R. Koehler. *Funding Acquisition:* I. Pierce, R. Koehler. *Investigation:* I. Pierce, R. Koehler. *Methodology:* I. Pierce, R. Koehler. *Project Administration:* I. Pierce, R. Koehler. *Resources:* I. Pierce, R. Koehler. *Software:* I. Pierce. *Supervision:* R. Koehler. *Validation:* I. Pierce, R. Koehler. *Visualization:* I. Pierce. *Writing – original draft:* I. Pierce. *Writing – review & editing:* I. Pierce, R. Koehler.

**Abstract** Measuring displacements of buried and faulted strata on strike-slip faults requires detailed 3D trenching excavations. Here we demonstrate a new methodology using co-registered, photorealistic 3D models derived from an iOS-based laser scanner and structure-from-motion photogrammetry to reconstruct stratigraphy and trace a displaced channel sequence across the Dog Valley fault in the northern Walker Lane. We present new geomorphic mapping observations and trenching results. Lidar data reveal a east-northeast striking fault trace that extends about ~25 km from just west of the Polaris Fault to the northwest flank of Peavine Mountain. Youthful fault scarps are visible along much of the fault. Clear lateral displacements are largely absent along the fault; however, right-stepping fault strands, sidehill benches, linear valleys and ridges, and alternating scarp facing directions are all consistent with left-lateral strike slip displacement. Stratigraphic and structural relations exposed in the Dog Valley fault trench show truncations of bedded fluvial and peat deposits and provide evidence for the occurrence of two Holocene earthquakes: the most recent earthquake postdates ~8 ka, and an earlier earthquake occurred between 8491–8345 cal. ybp. Based on 3D excavations of a channel margin, the most recent earthquake produced 115±30 cm of left-lateral displacement, corresponding with up to a M6.7 earthquake. Similar timing for the most recent earthquake on the Polaris fault which orthogonally intersects the Dog Valley fault may indicate rupture behavior similar to conjugate historic ruptures elsewhere in the Walker Lane.

**Non-technical summary** Here a new set of 3D imaging techniques is used to produce a 3D model of a series of interconnected trenches excavated across the Dog Valley fault near Lake Tahoe, California. The result allows for the accurate digital measurement of displacement of sediments across the fault. The fault is a left-lateral strike-slip fault in the Walker Lane, a zone of distributed shear that is parallel to the San Andreas fault. The fault intersects a neighboring strike-slip fault at a 90° angle, similar to other faults in the Walker Lane that have ruptured together during the last century.

## 1 Introduction

Paleoseismic studies of active faults are one of the primary methods for estimating the timing, recurrence, and size of prehistoric earthquakes – critical parameters for seismic hazard assessments (McCalpin, 2009). Typical paleoseismic studies combine shallow subsurface excavations ('paleoseismic trenches') with detailed surficial fault maps. These paleoseismic trenches aim to measure the fault displacement and timing of past fault ruptures. While fault displacement is readily measured from a single trench exposure across a dip-slip fault, an array of multiple trenches ('3D trenching') is required to find traceable subsurface piercing lines across a strike-slip fault (Marco et al., 2005; Rockwell et al., 2009; Hall et al., 1999). The standard method of documenting a series of 3D trenches consists of a plan

view map of the trench excavations and then a series of trench-wall-log diagrams. However, aligning these 2D diagrams so they can be visualized in a 3D space is not a simple task.

In recent years, trench-wall diagrams are increasingly constructed using Structure-from-Motion (SfM) algorithms to produce high-detail orthophoto mosaics of trench walls (Haddad et al., 2012; Bemis et al., 2014; Reitman et al., 2015; Delano et al., 2021). SfM relies on photogrammetric principles and many overlapping photographs taken from different positions to reproduce the 3D geometry and camera locations of a scene. Here we present a novel method that uses an Apple iOS laser scanner and SfM 3D modeling to generate a computer model of oriented and aligned high-resolution trench wall images. These aligned images form a readily viewed, true 3D stratigraphic/structural reconstructed model of a volume of faulted crust. This model can then be used for measuring fault displace-

Production Editor:  
Gareth Funning  
Handling Editor:  
Randolph Williams  
Copy & Layout Editor:  
Hannah F. Mark

Received:  
August 4, 2022  
Accepted:  
December 10, 2022  
Published:  
January 12, 2023

\*Corresponding author: ian@nevada.unr.edu

ments and exploring the fault and stratigraphic structure, not dissimilar to 3D seismic data.

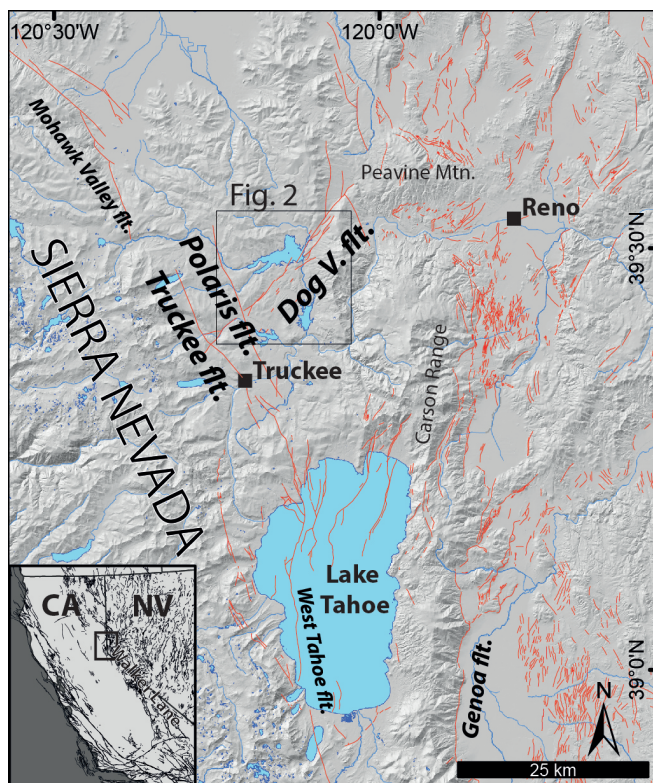


**Figure 1** Overview map of the Truckee Basin and surrounding region. Faults (abbreviated ft.) in red modified after the USGS Quaternary Fault and Fold Database (U.S.G.S., 2020) to reflect our updated mapping in the Truckee and Tahoe basins. Inset map shows the location with respect to California and Nevada and regional active faults.

We demonstrate the value of this method by employing it in a paleoseismic trench study of the Dog Valley fault within the Walker Lane tectonic province in northeastern California (Figure 1). The Walker Lane is characterized by a complex network of faults including range-front normal faults and conjugate right- and left-lateral strike-slip faults (Wesnousky, 2005). A number of historical earthquakes in the Walker Lane have been associated with conjugate or cross-fault ruptures (Smith and Priestley, 2000; Hatch-Ibarra et al., 2022; Barnhart et al., 2019). However, paleoseismic records in the Walker Lane are insufficient to evaluate how common these types of ruptures are along major faults. Analysis of static stress changes associated with the 2019 Ridgecrest earthquake sequence indicate that the M6.4 earthquake promoted slip in the M7.1 earthquake and triggered creep on the adjacent Garlock fault (Barnhart et al., 2019). Thus, the possibility that earthquakes might promote rupture on intersecting and/or other nearby faults has implications for future seismic hazards in the region.

Based on evaluation of our 3D trench model and field observations, we assess the earthquake history of the Dog Valley fault and estimate the displacement associated with the most recent seismic event. Additionally, we describe the geomorphic expression and length of the Dog Valley fault based on assessment of lidar hill-

shades and field reconnaissance. We then discuss the geometric and paleoseismic relationship of the Dog Valley fault with the intersecting Polaris fault and their significance in the context of conjugate strike-slip faulting and seismic hazards in the Walker Lane fault system. We conclude with a discussion of the utility of this methodology in comparison to alternative methods.

## 2 Geologic Setting

The Dog Valley fault is within the northern Walker Lane belt in northeast California and extends for ~25 km from north of Truckee, California to the north flank of Peavine Mountain near Reno, Nevada (Figures 1 and 2). The Walker Lane belt is a 100-km-wide zone of distributed faulting following the eastern margin of the Sierra Nevada mountains from ~35°–41°N latitude. The northern Walker Lane accommodates 10–15% (5–7 mm/yr) of the northwest oriented dextral shear between the Pacific and North American plates, with 2–3 mm/yr concentrated along its western margin, spanning the Truckee basin (Bormann et al., 2013, 2016; Pierce et al., 2021; Hammond et al., 2011).

The Truckee basin is the northernmost of a series of left-stepping en echelon basins that extend along the east side of the Sierra Nevada and accommodate dextral shear through a combination of oblique range-front normal faulting, vertical axis block rotations, and discrete strike-slip faulting (Pierce et al., 2021). Within the Truckee basin, this deformation is accommodated by the northwest-striking right-lateral Polaris fault (Hunter et al., 2011), the normal-oblique Truckee fault, and the conjugate northeast-striking left-lateral Dog Valley fault. The Polaris fault has produced Holocene earthquakes and has a minimum right-lateral slip rate of ~0.4 mm/yr (Hunter et al., 2011). A paleoseismic study by Melody et al. (2012) constrained the timing of the most recent Holocene earthquake on the Polaris fault to <7000 yr B.P., based on displacement of the Tsoyawata (Mazama) tephra. The Polaris fault intersects the western end of the Dog Valley fault with a nearly orthogonal geometry (Figure 2). The Truckee fault zone is mapped on the west side of the basin by Olig et al. (2005), but is not the subject of any other known published studies. The Truckee fault zone dextrally and vertically (down to the east) offsets late Pleistocene glacial deposits, suggesting it is an oblique right-lateral normal fault (Olig et al., 2005). Other nearby regional faults include the Mohawk Valley fault to the north (Gold et al., 2014) and West Tahoe fault to the south (Kent et al., 2005; Brothers et al., 2009; Dingler et al., 2009; Pierce et al., 2017) (Figure 1). The faults in the basin have generated several strong historical earthquakes (1966 M6.6 and two ~M6 earthquakes in 1914 and 1948; Olig et al., 2005) and numerous smaller earthquakes (e.g. 2021 M4.7), and pose a significant surface fault rupture and strong ground motion hazard to several water storage dams in the region and the communities of Truckee, California and Reno, Nevada.

Olig et al. (2005) is the most comprehensive study to date of the Dog Valley fault. In that study they report that the Dog Valley fault has produced 3.6–4.0 km



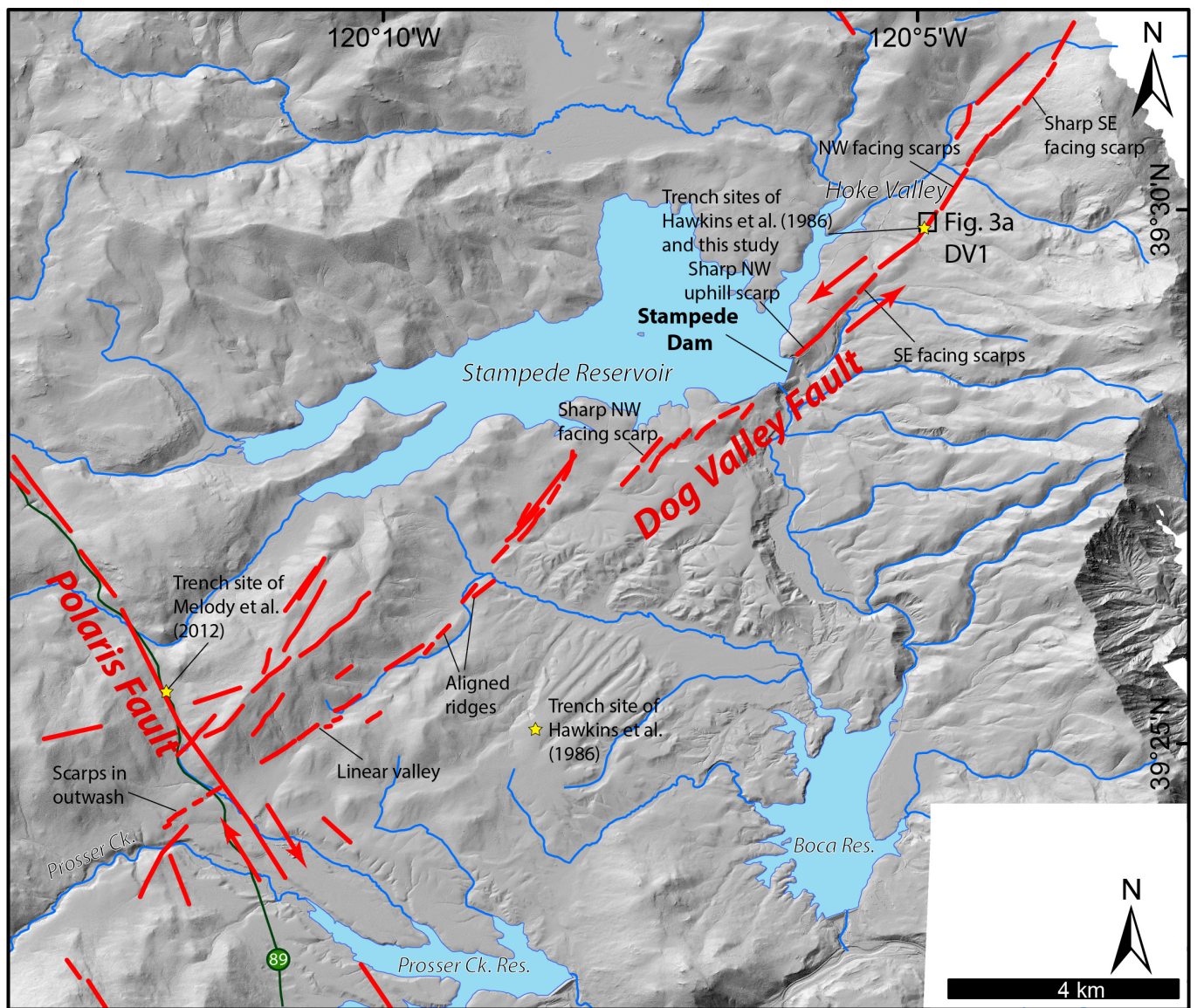


**Figure 2** Overview map of the left-lateral Dog Valley fault on a lidar hillshade basemap. Youthful fault traces are mapped in red. Previous paleoseismic trench sites marked with yellow stars. The surface trace of the Dog Valley fault intersects the Polaris fault at a near-orthogonal angle. The trench site for this study is located in Hoke Valley along the northeast portion of the fault.

of cumulative left-lateral offset since ~3 Ma. This implies an average long term left-lateral slip rate of ~1.3 mm/yr. They also describe a change of scarp morphology from prominent, primarily northwest-facing scarps along the northeastern portion of the fault zone to alternating facing and more subdued and scattered lineaments to the southwest. Along the fault trace they detail a number of features suggestive of strike-slip motion including side-hill benches, ridge-crest saddles, aligned linear drainages, and reversals in scarp directions.

The Dog Valley fault is reported to have been responsible for the 1966 M6.0 Truckee earthquake (Reed, 2014). However, features attributed to surface rupture during this earthquake are scattered and discontinuous. These features are more likely a result of shaking and may be considered lateral spreads in unconsolidated alluvial deposits, rather than surface rupture along the principle fault trace (Olig et al., 2005). Relocated hypocenters show that the Dog Valley fault forms a distinct lin-

eamment of ongoing seismic activity (Reed, 2014). The fault is absent from the geologic map of the Independence Lake and Hobart Mills quadrangles (Sylvester and Raines, 2013).

Hawkins et al. (1986) excavated two paleoseismic trenches across scarps thought to be associated with the Dog Valley fault (Figure 2). The first trench was excavated in Hoke Valley, adjacent to the site excavated in this study. The second trench was excavated across a linear drainage north of Prosser Creek Reservoir thought to be the surface expression of the fault responsible for the 1966 earthquake. Neither trench identified any evidence of late Quaternary fault rupture. Hawkins et al. (1986) may not have identified the fault in their Hoke Valley trench because of the amount of water flooding the trench.

### 3 Methods

#### 3.1 Fault Mapping

We mapped tectonic geomorphic features and fault traces along the length of the Dog Valley fault based on interpretation of lidar hillshade maps and field reconnaissance. The main trace of the Dog Valley fault is visible in the 2014 Tahoe National Forest lidar imagery (OpenTopography, 2017). Mapping along the Dog Valley fault indicates that it is characterized by right-stepping en echelon fault strands expressed as subdued geomorphic features including both northwest- and southeast-facing scarps, closed depressions, aligned linear ridges, springs, and sidehill benches (Figure 2).

The northeastern-most part of the fault cuts across the northwestern flank of Peavine Mountain near Reno, Nevada (Figure 1). Southwest from Peavine Mountain the fault forms a sharp sidehill bench and aligned ridge before entering Hoke Valley (Figure 2). In Hoke Valley, a series of springs and 1-2 m high northwest facing scarps along the base of the range front that bounds the southeastern margin of the valley mark the location of the fault. At the southwest margin of Hoke Valley, the fault cuts across topography forming a series of linear ridges, sidehill benches, and both northwest- and southeast-facing scarps before approaching the Stampede Dam.

The lidar data reveal that the trace of the Dog Valley fault extends through the Stampede Dam (Figure 2). Our field observations indicate that strands of the Dog Valley fault offset Miocene andesite flow breccias and tuff breccias exposed in a roadcut immediately northeast of the dam, and a sharp uphill facing fault scarp extends across a bench on the hillside above this roadcut.

Southwest of Stampede Dam, the fault is clearly expressed by sharp scarps and linear ridges that extend along right-stepping en-echelon strands. The fault then continues along a linear ridge and valley; however, in this area tectonic geomorphic features become less pronounced and we were unable to precisely locate the fault in the field. Just west of the Polaris fault and Highway 89, the fault appears to terminate, forming a subtle southeast facing scarp in glacial outwash deposits along Prosser Creek.

#### 3.2 Trenching Excavation

A series of interconnected 3D paleoseismic trenches (site DV1) were excavated on the southeast margin of Hoke Valley, approximately 3 km northeast of Stampede Reservoir where the Dog Valley fault forms a 2-m-high northwest facing scarp across the mouth of a small alluvial valley (Figures 2, 3a). An apparent left deflection of an ephemeral stream channel adjacent to the trench occurs across the fault at this site.

In total, 16 exposures were imaged, covering a volume roughly 2 m across the fault zone, 4.5 m along the fault, and 2 m deep (Figure 3c). The across fault exposures are labeled from northeast to southwest A01-A14, while the fault parallel exposures are labeled P1 and P2. Initially, a single 11 m long, 80 cm wide, 2 m deep, vertical walled excavation was produced perpendicular to the fault scarp. Both walls of this excavation

(A07 and A08) were carefully cleaned, examined, and described using standard paleoseismic methods (Figure 4). Both walls were then imaged using the methodology described in the following section. After this initial excavation, approximately 2 m of the northeast wall of the trench, centered on the fault zone, was expanded ~20 cm, parallel to the initial excavation. This new exposure (A06) was then cleaned and imaged. This process was repeated for a total of 6 new exposures of the northeast wall (A01-A06), extending 1.5 m northeastward along strike. This process of progressively expanding this cross fault trench produced a fault-parallel exposure on the southeast side of the fault (P2). Next, a second fault parallel trench was excavated (P1), extending from approximately 1 m northwest of the fault exposed on the original southwest wall, for 2.75 m to the southwest. From the southwest end of this fault-parallel exposure, 6 more 2-m-wide cross fault exposures were created (A09-A14), working from southwest to northeast back towards the original southwest trench wall. Finally, cleaning the orthogonal southeast margin of these exposures extended P1 by 2.5-m to the southwest. Orthoimages of each exposure are provided in Figure 5 and in a repository, see the data availability statement for details.

#### 3.3 Trench Wall Imaging

Prior to imaging each trench exposure, the trench walls were cleaned using scraping tools and colored flags were nailed to the walls to mark prominent stratigraphic layers. In most exposures, a short level string line was installed between two nails for referencing. The trench walls were then photographed using a Google Pixel 2 cell phone camera fixed to a 1.5 m long extension pole and a Bluetooth remote shutter trigger. Photographs were taken in portrait orientation, orthogonally to the wall, and approximately 1 m away from the trench wall. Photographs were taken in a 'lawn-mower' pattern, with first a descending vertical column of overlapping photos, then a short (~0.5 m) lateral step, then an ascending vertical column of overlapping photos, then a short step, and so on, until the entire trench wall was photographed. Photos were uploaded to a laptop in the field and processed into an orthoimage using the Agisoft Metashape photogrammetry software (Agisoft LLC, 2022). It is important to field check image processing as, for unknown reasons, a set of photos may fail to properly align and may need to be re-photographed. After ensuring that an orthoimage could successfully be produced, the trench wall was lidar scanned using the SiteScope app on a 2020 Apple iPad Pro in 'high detail' mode. Lidar scanning followed a similar acquisition methodology as the photography, consisting of slowly following a 'lawn mower' pattern orthogonal to the trench wall until the entire wall was covered. In addition to just the wall of interest, each lidar scan also covered parts of the trench network that were not modified during progressive excavations.



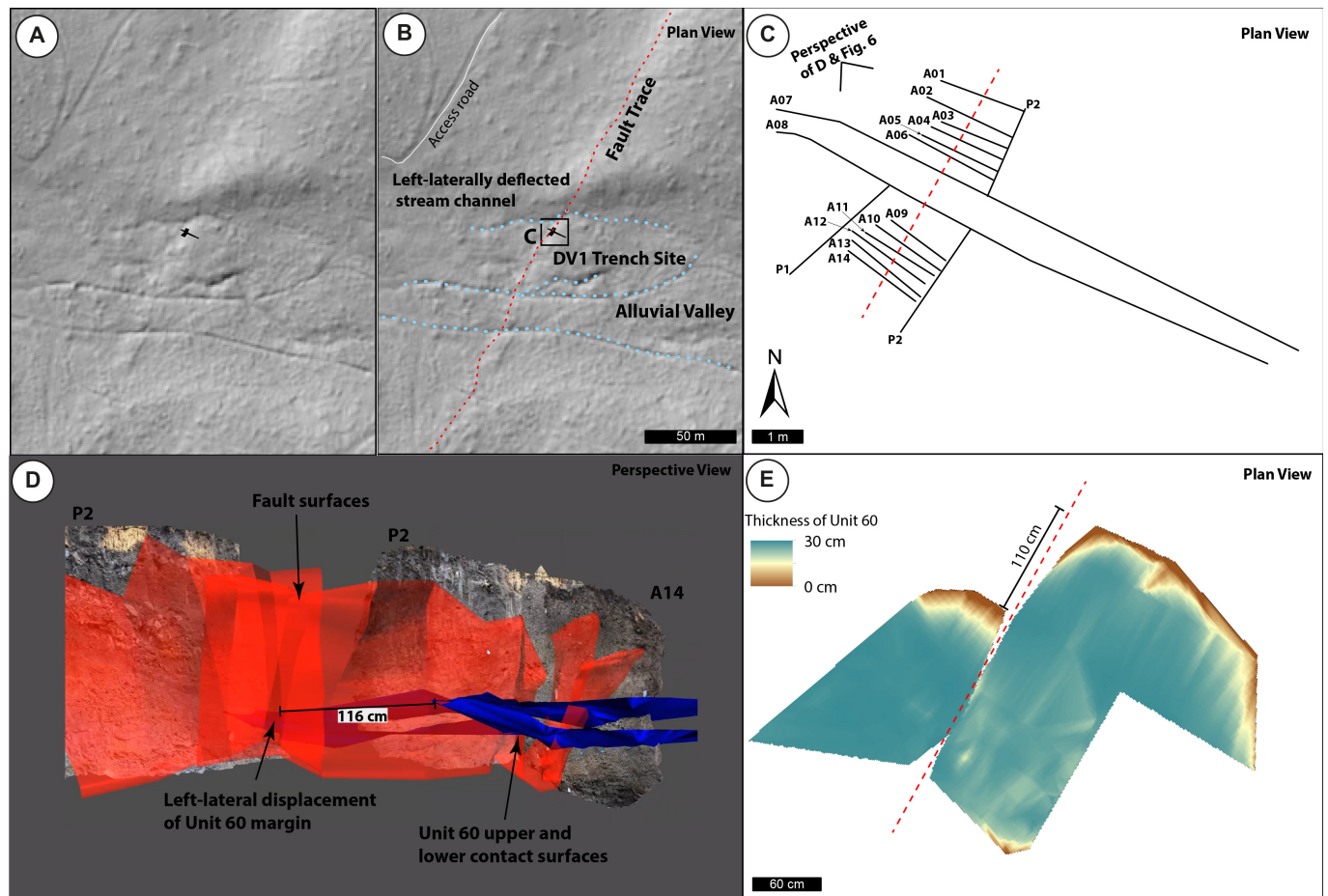


**Figure 3** (A) Lidar hillshade and (B) interpreted hillshade of DV1 trench site in Hoke Valley. Dashed red line is fault and dashed blue lines are channels. Note the left-lateral offset of a small channel at this site. (C) plan view map of trench excavation network. Each line shows the location of the trench walls imaged and reproduced in Figures 4–7. The view orientation of (D) and Figure 6 is indicated with brackets. (D) oblique 3D model of stratigraphic reconstruction of Unit 60 (blue) and faults (red). The 116 cm offset of the margin of the Unit 60 channel is shown. (E) Plan view isopach map of Unit 60 showing 110 cm left lateral offset of the channel margin.

### 3.4 3D Model Construction

For clarity, prior to describing the construction of the 3D model of DV1, we first define and describe the different categories of 3D data we use. A point cloud consists of many individual points that each have an x, y, and z coordinate, and each point may have a photo-based visual color or other data such as reflection intensity. Common point cloud formats include .laz, .las, and .xyz. In contrast, a 3D surface model is typically a triangulated or polygonised surface composed of many connected polygons that together form the surface of a 3D object. 3D surface models can be constructed from a point cloud using a meshing algorithm. 3D models are often textured with photo images to look realistic. Common 3D file formats include .obj, .stl, .3ds, and .glTF. Both point clouds and surface models are different than ‘2.5D’ raster formats common to geospatial software such as digital elevation models (DEMs) or orthoimages/orthophoto mosaics (e.g. .tif, .jpg, etc.). These ‘2.5D’ raster formats are 2-dimensional grids where each grid cell contains data (such as photo-color, elevation, etc.).

In this study we do not attempt to formally assess the accuracy of the iOS laser scanner, but others’ work

shows that its accuracy decreases with increasing size of the object or scene being scanned (Luetzenburg et al., 2021). Luetzenburg et al. (2021) compared an iOS survey of a 130-m-long by 10-m-high sea cliff to a georeferenced SfM survey and found a mean error of 11 cm, while for smaller objects (~50 cm/site) errors were <1 cm, with a minimum size threshold of ~15 cm before accuracy decreases. Our own informal testing of the iOS lidar found that measurements of distances ranging from ~1–3 m made in lidar scans were generally within ~2 cm of those made by hand with a tape measure. While in this study we use a 2020 iPad Pro due to its comparative low cost and ease of use, other close-range handheld laser scanners may be suitable for this workflow. Ideally the scanner used should capture photo RGB values of points (or create photo-textured 3D surface models); otherwise, control points will need to be targets that sufficiently contrast in intensity to be identifiable. Finally, data from whichever scanner or app is used should be readily exportable in a common 3D format.

At the time of the field study, the SiteScope app was the only iOS app that we were aware of that could create a photo-colored point cloud. Since this work was completed, other apps have been developed that can create

more realistic looking photo-textured 3D models (Luetzenburg et al., 2021). With any of these iOS lidar apps (or with other laser scanning systems) this same workflow should be applicable.

First, using the freely available software CloudCompare (GPL Software, 2022), all 3D iOS scans (in this case we use point clouds, but 3D surface models work too) are aligned into a common reference frame (Figure 6b). In our case the reference frame is arbitrary (i.e., local coordinates in meters), but one could align the local reference frame to a global reference frame using control points surveyed with a differential GPS (dGPS). Alignment between iOS scans is achieved by finding unchanged areas within the excavation network that have common reference points that can be identified across multiple excavation models. Ideally these reference points are high contrast flags placed on stable areas of the trench walls. A minimum of 3 points must be identified to translate and rotate a model into alignment, but typically 15-30 points were used. Points should be distributed throughout the space for best results.

Next, using Agisoft Metashape, photos of each trench wall are processed into photo-textured 3D surface models (not 2D orthophoto mosaics; Figure 6c). These are then cropped to only contain the area of interest and then imported into the model in CloudCompare (here using .obj format). Each of these photo-textured 3D models is then warped, scaled, rotated, and fit to the corresponding lidar trench scan (point clouds), using a similar method of identifying common reference points between the lidar scan and the photo-textured 3D surface model. The photo-textured 3D models are used as they are much higher resolution than can be produced using the currently available iOS laser scanning apps. The result is a correctly-scaled high-detail 3D model of all of the trench exposures, where different exposures can be turned on and off and measurements can be made. The result has the added advantage of being insensitive to irregular trench wall surfaces. Curving, sloping, benched, or other non-planar trench walls are not forced to be flat as they would be with a more traditional orthoimage representation.

### 3.5 3D Stratigraphic-Structural Interpretation

We used three different methods for structural analysis, with the goal of measuring displacement of units across the fault zone. First, 2D stratigraphic models (logs) of each exposure are developed with key units correlated between different exposures (Figure 4). In each exposure, contacts appear as lines on the trench wall. Using CloudCompare, a series of points representing each contact-line are manually extracted from each exposure, independently on each side of the fault. For example, if a given contact is visible in 8 exposures, and on both sides of the fault zone, 16 sets of points would be extracted. The extracted points for each contact of interest on every exposure are then merged into a point cloud, resulting in two point clouds representing each contact surface (one on each side of the fault). The same process is repeated for the fault surfaces. These

point clouds are then used to build 3D surfaces represented by Triangular Irregular Networks (TINs). Once TINs representing contact surfaces are created, two different methods can be used to determine a fault offset. First, if two contact surfaces intersect, this intersection may form a piercing line that can be traced to a piercing point on the fault surface, on either side of the fault, and then an offset measured between these two piercing points (Figure 3d). For the second method, the thickness of a unit between two contact surfaces can be plotted in plan view as an isopach map, and the offset in thickness can be measured across the fault (Figure 3e). The isopach map in Figure 3e was created by using the TIN to raster tool in ArcGIS for two contact-surfaces that bound a unit and then differencing the resulting rasters.

A third, less precise method is also used to estimate fault offset. Each photo-textured 3D model can be cut along the fault zone into two models. One side of the fault in one model is then compared to the other side of the fault in other models to find the qualitatively best matching stratigraphy (Figure 7). This effectively serves to 'backslip' the fault. When a fit is determined, the distance between matching contacts can be measured in the 3D space, again resulting in a slip vector. While this method is less precise, it serves as a useful validation and check on the prior methods.

## 4 Paleoseismic Results

The trench exposed a sequence of low energy interbedded fluvial overbank sands, silts, and peats (buried soils), with cobble and gravel lenses, and a 1-2 m thick modern meadow soil (Figure 4). These deposits are faulted by a steeply dipping narrow fault zone that reaches nearly to the ground surface. In each exposure, 1-3 main splays of this fault are visible in an ~20 cm wide zone that generally spread upwards forming a weak flower structure. There is negligible vertical deformation across this fault, but in some exposures the strata on the southeast side of the fault either warp slightly down (A11-A14) or slightly up (A04-A08). Strata are mismatched across the fault in most exposures. In the logs, we focus on a clearly traceable sequence of interbedded sand and silty peat layers that can be traced through exposures A04-A14 and P1 and P2. From top to bottom these sand beds are mapped as Unit 50, 60, and 70, and a mottled silt unit 80. Exposure P2 contains a clear sand dike extending from Unit 50 to the modern soil, likely a result of coseismic liquefaction (Figure 4).

In most exposures there is only evidence for the most recent earthquake (E1), based on the primary fault zone that extends to the soil. This event also produced the sand dike in P2. The northeast upper margin of the Unit 50, 60, and 70 sandy channel beds form piercing lines that can be traced across the fault zone (Figure 6). Figure 3e shows an isopach map of Unit 60. These units are left-laterally offset across the fault zone. Left lateral displacements measured from the isopach method (Figure 3e) and 3D piercing point reconstruction method (Figure 3d) of the northeast margin of Unit 60 are 110 and 116 cm, respectively. Using the visual back slip method described above produces slip estimates be-



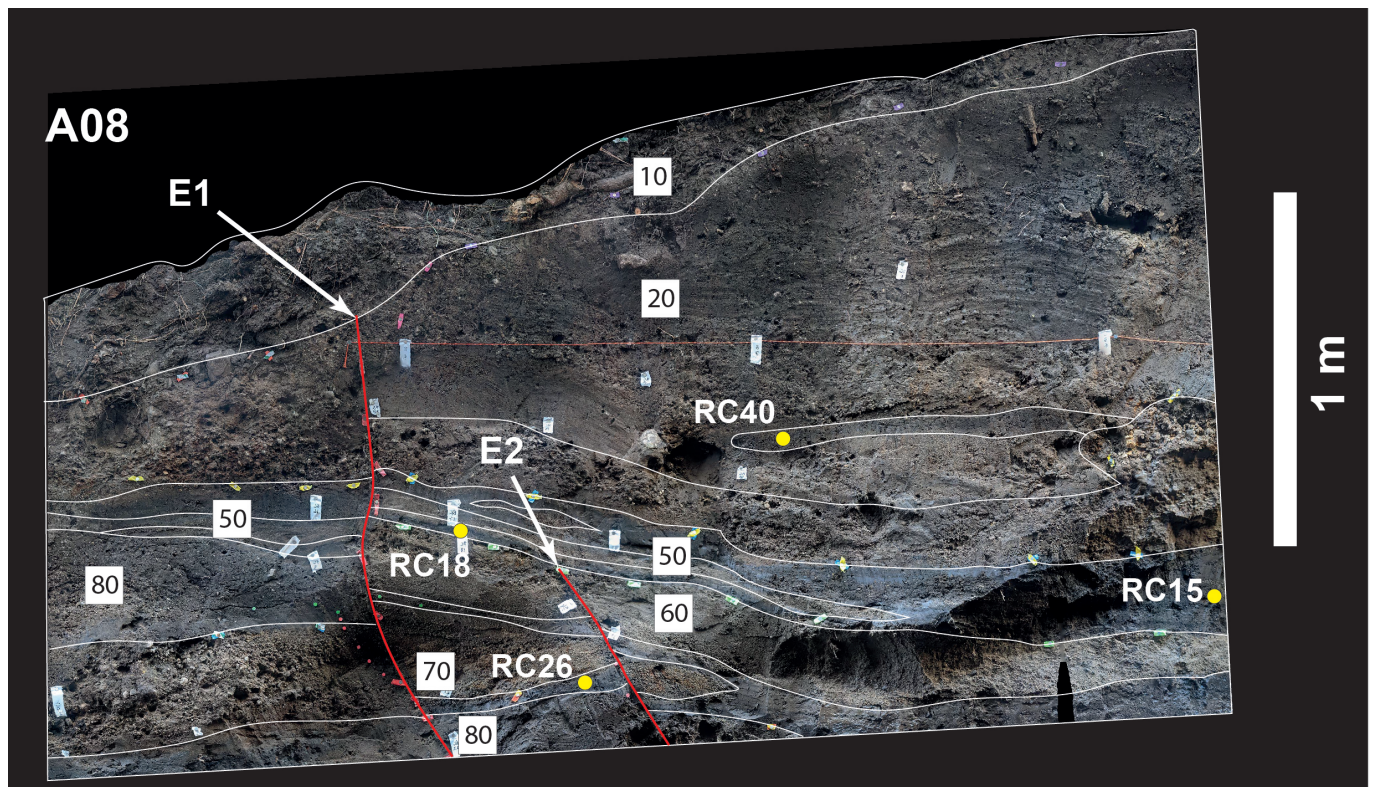


**Figure 4** Annotated trench orthoimage showing unit contacts (white lines), radiocarbon samples (yellow dots), and faults (red lines). Upward terminations of events E1 and E2 are indicated with white arrows. See Table 1 for radiocarbon ages and Table 2 for unit descriptions.

tween 88–145 cm (Figure 7). The total range of left-lateral displacement from these various methods is  $115 \pm 30$  cm. We estimate this uncertainty based on the total range of measurements. This uncertainty seems reasonable as it approximates the limit of our fault-parallel resolution based on the average spacing between adjacent excavations.

Evidence for an earlier earthquake (E2) consists of a single upward terminating fault strand in each of exposures A08 and A11–A14 (Figure 5). These fault strands terminate in Unit 60 in A08 and below Unit 70 in A11–A14. In exposure A08, the fault strand is buried by Unit 50. Strata below Unit 60 do not match as well across the fault when visually back-slipped (Figure 7), consistent with increased displacement from an earlier event.

#### 4.1 Event Timing

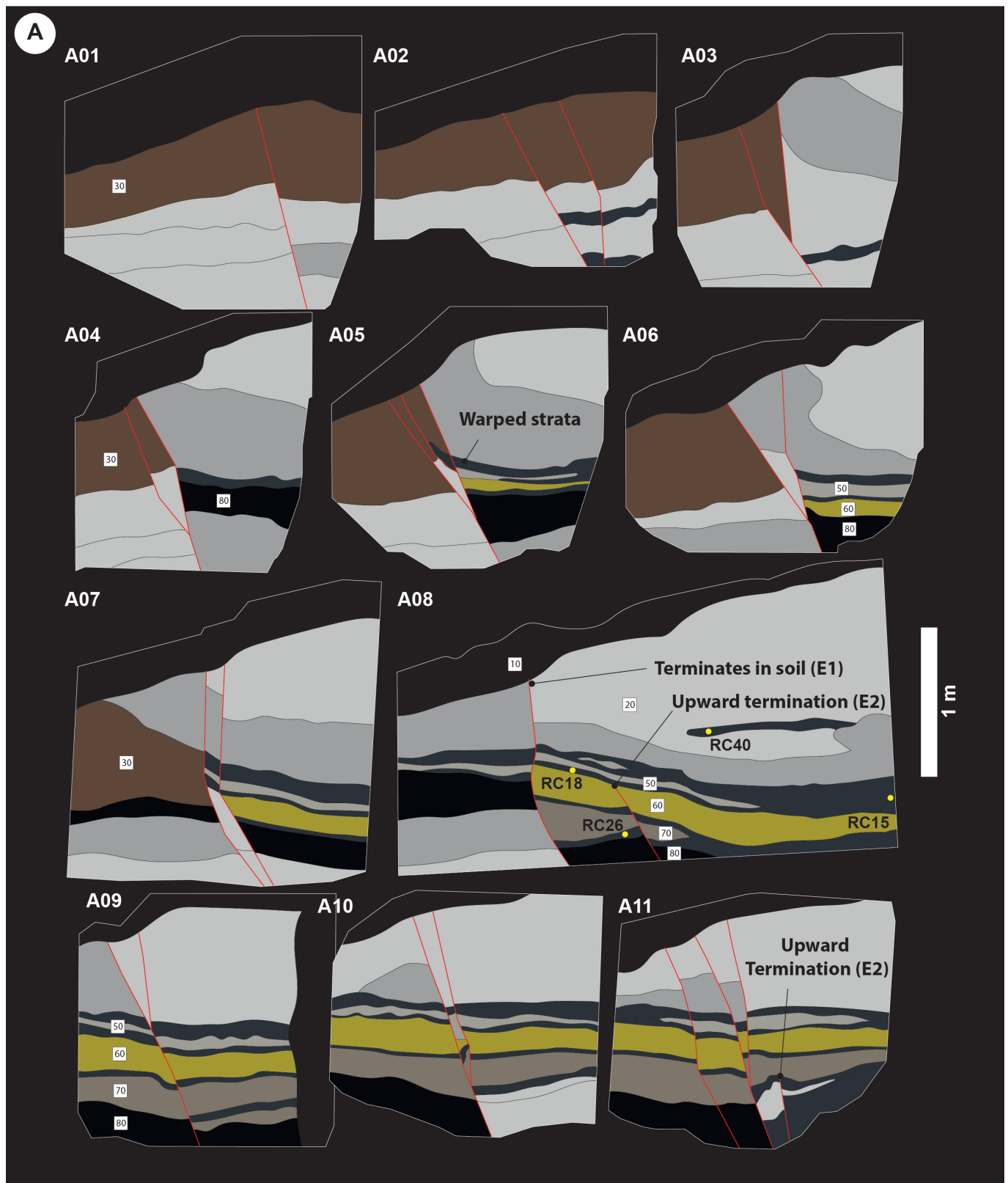
Radiocarbon dating was used to determine the ages of 5 total samples of peat, charcoal, and wood extracted from trench walls A08 and P1. Samples were processed and analyzed at Beta Analytic laboratories. Resulting ages are listed in Table 1. OxCal v4.4 (Bronk Ramsey, 1995) calibrated ages range from 8998–8031 cal. ybp. Sample RC18 is slightly out of stratigraphic order so is discarded from the following analysis. Ages RC43 (P1) and RC26 (A08) predate the older event E2, based on the upward terminating fault in Unit 60 which is buried by Unit 50 in exposure A08. Samples RC15 and RC40 (A08) are younger than E2 and predate the most recent event, E1. No radiocarbon samples postdate E1. By calibrating the ages of these samples we build a sequence model in

OxCal using the stratigraphic positions of the samples and event horizons to determine the timing of these two earthquakes. The resulting limits on event timing are E1: younger than 8051 cal. ybp, and E2: between 8491–8345 cal. ybp (Figure 8). Approximately 1 meter of fine-grained sediment (Unit 20) buries the layer that contains sample RC40 and was faulted in earthquake E1. Given the distribution of ages and the thin peat soils in the lower part of the exposure, sedimentation rates at the site were relatively high in the early Holocene, likely a reflection of the unvegetated post-glacial landscape. As the landscape stabilized in the mid-Holocene, sedimentation rates slowed resulting in the accumulation of Unit 20. We could not definitively track the upward termination of the fault or the sand dike in P2 into the weak late Holocene soil that developed into Unit 20 (Unit 10). These observations suggest that E1 may have occurred within the several thousand years after 8310–8031 cal. Ybp.

#### 4.2 Paleoearthquake magnitude estimated

If the full mapped 25 km fault length ( $L$ ) ruptured with  $115 \pm 30$  cm of displacement ( $D$ ) and a 17 km fault width ( $W$ ) (assuming a vertical fault and 17 km seismogenic thickness from Ruhl et al. (2020)) the moment magnitude can be calculated using the following equation (Hanks and Kanamori, 1979):

$$M_w = \frac{2}{3} \log(3 \times 10^{11} \times L \times W \times D) - 10.73 \quad (1)$$



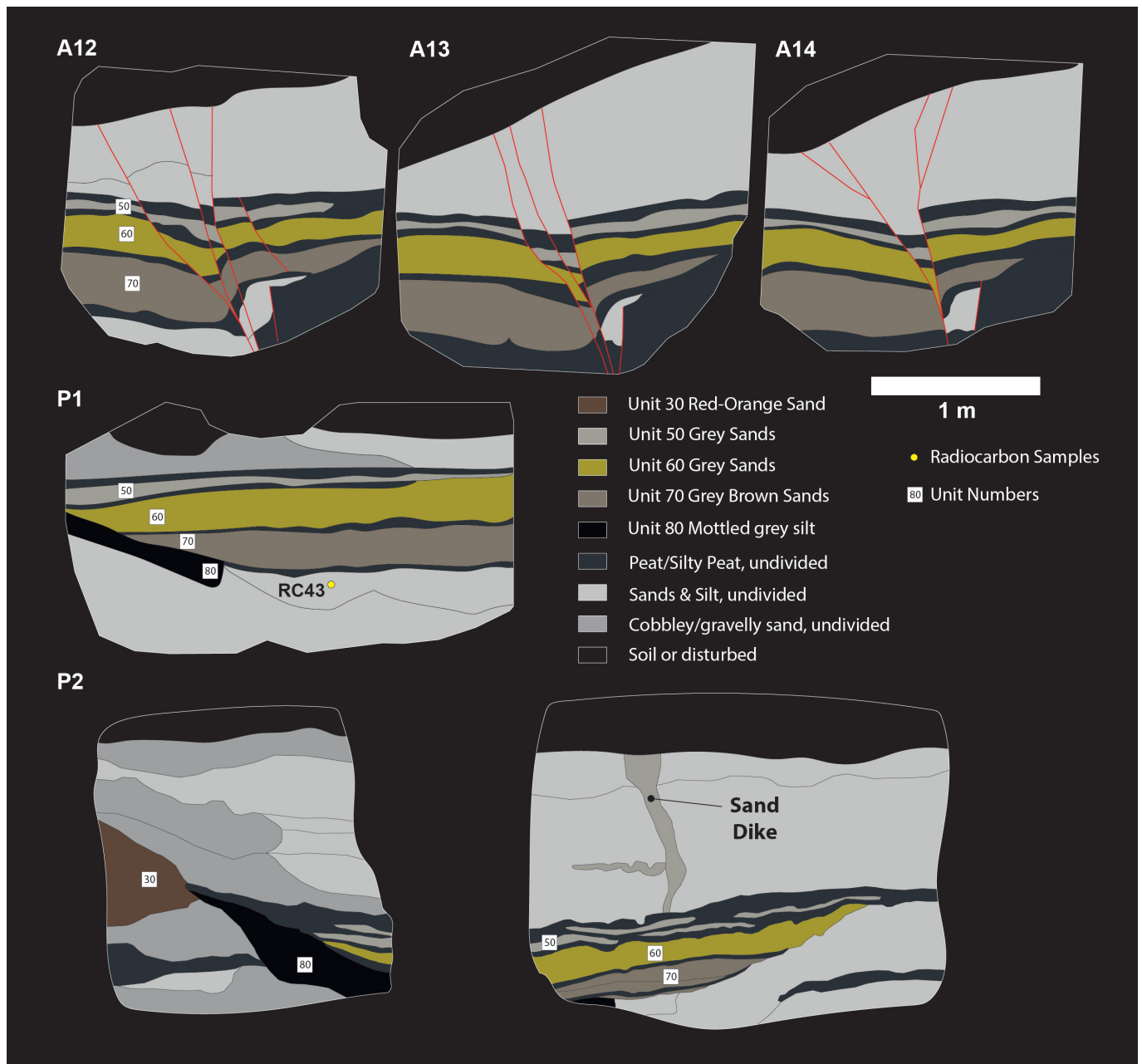
The resulting magnitude is  $M_w 6.7 \pm 0.1$ . Both this magnitude estimate and the measured geologic slip are similar to those estimated from empirical relations of average displacement-fault length and magnitude-fault length, based on other strike-slip earthquakes and assuming a 25 km rupture length (Wesnousky, 2008).

## 5 Discussion

### 5.1 Tectonic Role of the Dog Valley Fault and Conjugate Faulting in the Walker Lane

One of the defining characteristics of the Walker Lane and Eastern California Shear Zone is the presence of conjugate right- and left-lateral faults (Wesnousky, 2005). The Dog Valley fault lies north of the Carson domain in the Walker Lane, a region comprised of a se-





ries of east-dipping normal fault bounded basins that are oriented oblique to the overall northwest structural grain of the Walker Lane (Wesnousky et al., 2012; Pierce et al., 2021). Many of these north-striking normal fault bound basins are paired with an east- or northeast-striking left-lateral strike-slip fault (Li et al., 2017), and several contain northwest-striking strike-slip faults (Pierce et al., 2021). This network of faults works together to accommodate the ~5-7 mm/yr of northwest directed dextral shear in the Carson domain (Pierce et al., 2021).

The Dog Valley fault and the Polaris/Truckee faults share a similar geometric relationship to these other paired faults and may serve a similar role in the accommodation of northwest directed dextral shear. Our fault mapping indicates that the left-lateral Dog Valley fault zone intersects the northwest-striking right-lateral Polaris fault at a nearly orthogonal angle (Figure 2). Our interpretation of trench DV1 along the Dog Valley fault indicates the occurrence of at least one earthquake that

occurred after 8051 cal. ybp that was associated with  $115 \pm 30$  cm of left-lateral displacement, and a prior event that occurred between 8491-8345 cal. ybp. Comparing this result to previously reported earthquake timing data from the conjugate Polaris fault indicates that the most recent earthquake along both faults post-dates ~7-8 ka (Melody et al., 2012). Thus, the geometric and paleoseismic relations indicate that the two faults may be kinematically linked and that ruptures along each fault could occur over a short period of time and possibly contemporaneously in a conjugate earthquake sequence.

Multiple historical earthquakes in Southern California, the Eastern California Shear Zone, and the Walker Lane provide examples of conjugate faults rupturing either simultaneously or closely spaced in time (minutes to decades). These include, in southern California, the 1987 Superstition Hills earthquake sequence ( $M_s 6.2$  and  $M_s 6.6$ ) and the  $M_w 6.4$  Big Bear earthquake (Jones and Hough, 1995; Hudnut et al., 1989). In the Walker



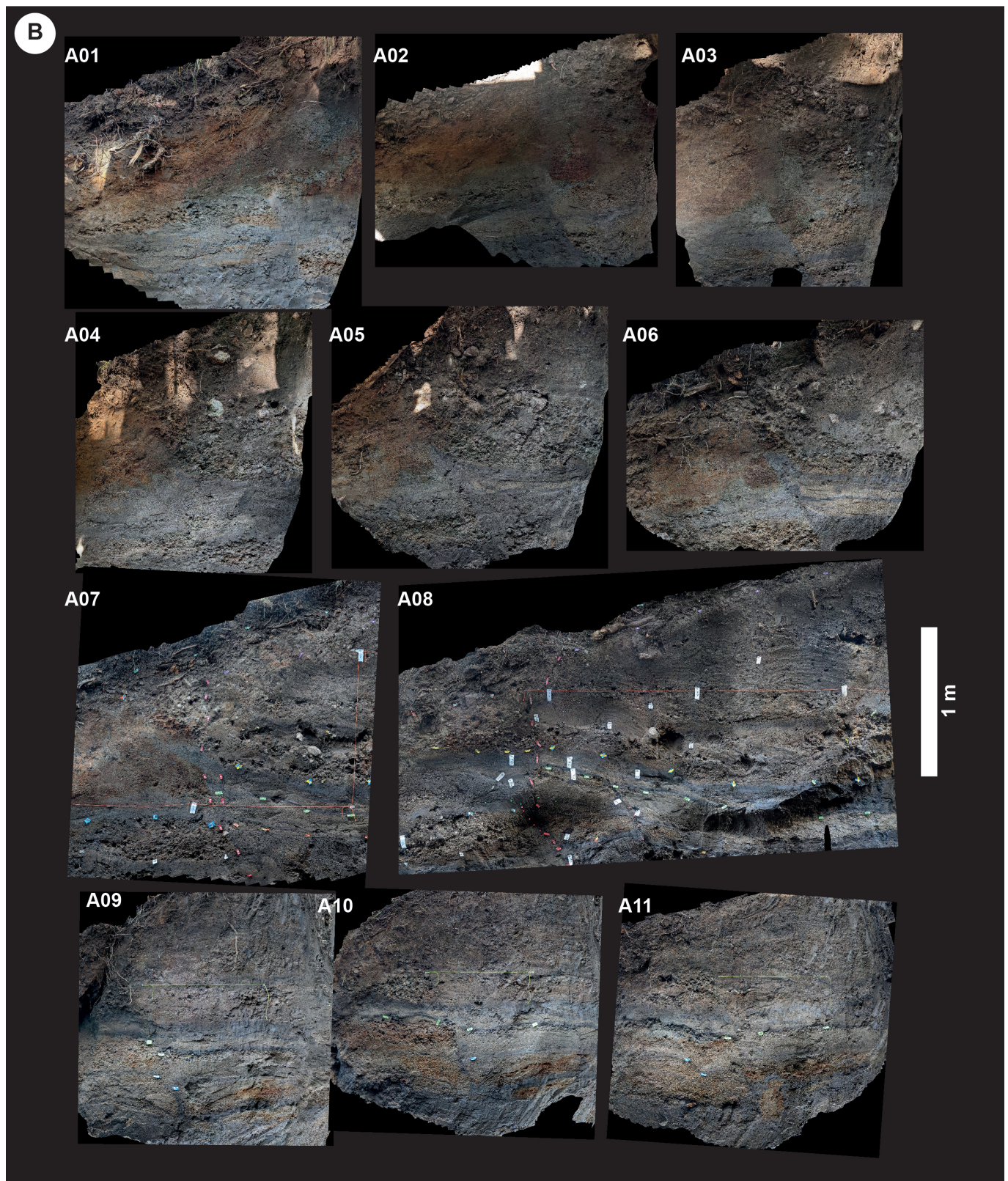


**Figure 5** (A) Interpreted trench logs. Faults in red, radiocarbon samples yellow dots. (B) Trench orthophotos. Evidence of the most recent event (E1) consists of a clear fault that extends into the modern soil and a sand dike in slice P2. The earlier event (E2) is evident by an upward terminating fault strand in slices A08 and A11-14.

Lane, conjugate earthquakes include the 1986 Chalfant earthquake ( $M_w$ 6.3 and  $M_w$ 5.7), the 2015 Nine-Mile Ranch (three  $M_w$ 5.4-5.6 events), and the 2019 Ridgecrest earthquake ( $M_w$ 6.4 and  $M_w$ 7.1) sequences (dePolo and Ramelli, 1987; Smith and Priestley, 2000; Hatch-Ibarra et al., 2022; Barnhart et al., 2019). As observed from

surface ruptures, moment tensor solutions, and focal mechanisms, all of these examples involved rupture on intersecting conjugate northeast- and northwest-striking faults or fault planes.

Aside from the Big Bear earthquake, in each of these examples, the east or northeast-striking left-lateral



Sample Name	Material	D14C	δ13C	Radiocarbon Age (ybp)	Calibrated Age <sup>a</sup> (cal ybp)	OxCal Modeled Age <sup>b</sup> (cal ybp)
RC15	Detrital charcoal	-610.30 ± 1.46 ‰	-26.2 ‰	7570 ± 30	8417-8343	8414-8223
RC18	Charred material from peat	-630.15 ± 1.38 ‰	-23.3 ‰	7990 ± 30	8998-8655 (94.2%) 8665-8655 (1.2%)	-
RC26	Plant material from peat	-616.08 ± 1.43 ‰	-28.7 ‰	7690 ± 30	8543-8411	8544-8413
RC40	Organic sediment from peat*	-599.98 ± 1.49 ‰	-24.7 ‰	7360 ± 30	8310-8031 (11.4%) 8212-8031 (84.1%)	8309-8031
RC43	Wood	-613.68 ± 1.44 ‰	-26.8 ‰	7640 ± 30	8520-8376 (8.3%) 8485-8376 (87.1%)	8522-8389

Samples analyzed by AMS at Beta Analytic Testing Laboratory, Miami, Florida, USA

All samples pretreated with acid/alkali/acid washes unless otherwise noted

\*Treated with acid washes only

<sup>a</sup>Independently OxCal calibrated ages using the IntCal 20 curve

<sup>b</sup>Ages modeled in stratigraphic sequence using OxCal as described in text

**Table 1** Radiocarbon lab results and modeled ages for samples from the DV1 trench.

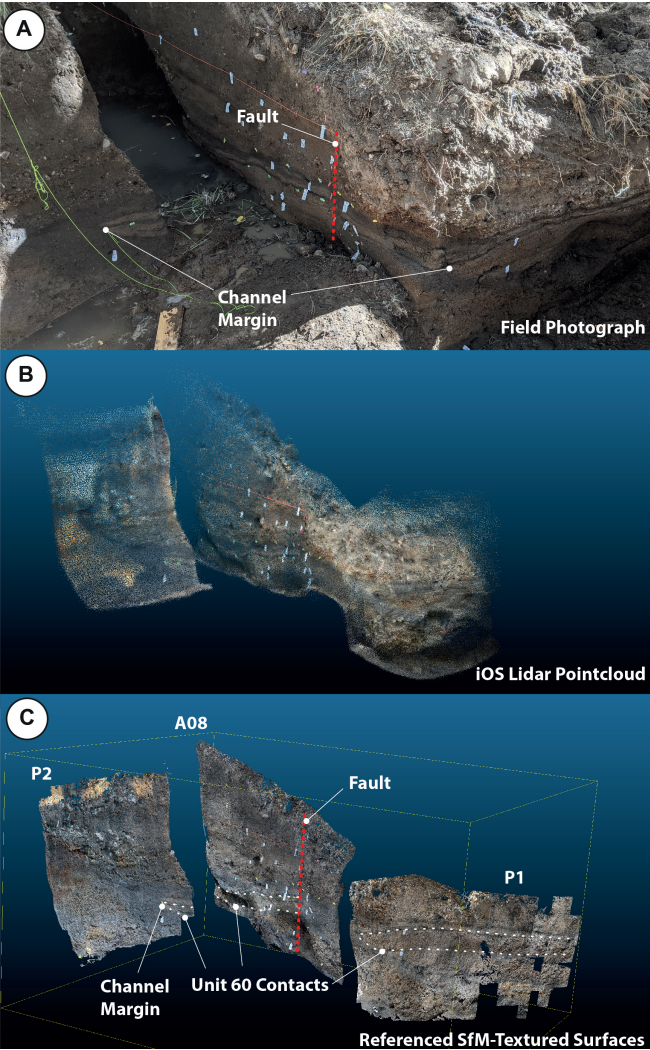


**Figure 6** Images showing how the iOS Pointcloud (B) and SfM-textured surfaces (C) are combined to reconstruct the original trench in photo in (A). Note the prominent channel margin sequence (Unit 60) that is displaced across the fault

right-lateral fault ruptures. Each of these examples of ruptures either forms an ‘L’ pattern or ‘T’ pattern in map view, with either one or both faults terminating at or within a few kilometers of the intersection point, and none form a ‘X’ pattern, with both ruptures continuing far beyond the intersection. The Superstition Hills and Nine-Mile Ranch sequences all have an ‘L’ pattern. The Big Bear, Ridgecrest, and Chalfant sequences each have a ‘T’ pattern, and in these examples, the fault that crosses the intersection (the top of the ‘T’) is the northwest-striking right-lateral fault. The Dog Valley and Polaris faults form a ‘T’ pattern with scarps of the Dog Valley fault extending for a few hundred meters southwest of the intersection and 25 km to the northeast (Figure 2). The Polaris fault extends ~14 km north and south from its intersection with the Dog Valley fault. This geometric relationship is similar to other historic ruptures in the Walker Lane, as well as the patterns associated with the 1968-1997 Dasht-e-Bayaz and 2010–2011 Rigan, Iran earthquake sequences (Walker et al., 2011, 2013; Rezapour and Mohsenpur, 2013; Barnhart et al., 2013), providing additional support to the possibility that they may rupture in a conjugate sequence.

Barnhart et al. (2019) indicated that Coulomb stress changes associated with the Ridgecrest earthquakes promoted creep on the nearby Garlock fault. Their analysis indicates that surface creep was induced over distances of ~20-25 km and may have encouraged a future rupture of  $M_w$  6.7-7.0. Although the Coulomb stress changes from a potential Dog Valley/Polaris fault rupture have not been investigated, their potential influence on the nearby Truckee, Mohawk Valley, and West Tahoe faults should be considered in future seismic hazards assessments.

Together, these observations show that conjugate fault ruptures may pose an underappreciated hazard in the Walker Lane and elsewhere. Further modeling and geologic studies should be developed to explore the past rupture histories on conjugate faults, the relative magnitude of contemporaneous ruptures, their influence on

fault ruptures preceded the north or northwest-striking

Unit #	Lower Contact	Upper Contact	Grain Size	Color	Description
10	Wavy/ gradual	n/a	Silt & sand	Gray/ brown	Surface soil, A-Bw horizon. Meadow environment w/ grass and many roots.
20	Sharp, wavy	Wavy/ gradual	Sandy silt to clay-silt w/ gravel	Brown with weak orange mottling	Generally massive. Crude defined layers. Contains channel stringers of gravelly sand. Stringers of gravel have rounded pebbles up to 3 cm. Some crude layers of darker organic material.
30	Sharp	Gradational	Gravelly sandy silt	Red/rusty orange & gray mottled	Massive gravels up to 4 mm. Subtle discontinuous gravel bedding near the base.
50	Sharp/ interbedded	Sharp, wavy	Peat, Silt & clay w/ interbedded sand lenses	Black	Very sticky, very dark black, decomposed organics rich, super soft. From top to bottom, organic silt, interbedded clean sand, prominent organic silt at base. Sand interbed: gray/brown, clean sand. Single grain structure, mostly medium grained sand. Forms small lenses within 50.
60	Wavy/sharp	Wavy/sharp	Medium sand	Gray	Bedded sand with coarse grained single grain sand to fine grained silty sand. Also contains centimeter thick organic silts in discontinuous lenses.
70	Wavy/sharp	Wavy/sharp	Medium sand	Gray	Bedded sand with coarse grained single grain sand to fine grained silty sand. Also contains centimeter thick organic silts in discontinuous lenses.
80	-	Sharp	Peat	Black	Very sticky, very dark black, decomposed organics rich, super soft.

**Table 2** Unit descriptions for stratigraphic deposits exposed in the trench.

the occurrence of earthquakes on nearby faults, and their impact on seismic hazard assessments.

## 5.2 Assessment of utility of iOS scanning method and comparison to prior methods

Properly scaling and referencing a SfM model into real-world units and coordinates requires that either the precise camera locations or the precise locations of control points in the scene be known. Without control points or camera locations, SfM models may appear accurate to the eye, but will be in arbitrary units and can suffer from bowl effects. Bowl effects are common artifacts towards the edges of SfM models where the model gradually warps towards the direction of the cameras, forming an overall concave shape (e.g., Jaud et al., 2019). In an SfM model of a trench, this often results in the ends of the trench warping towards the viewer. A bowl effect is evident in the trench model in Figure 4C of Delano et al. (2021), where the two ends of the trench have greater errors than the center when compared to the model referenced to a total station survey. Bowl effects can be particularly pronounced in very long shallow

trenches and can be problematic as they cause the geometry of the trench (and thus photo projections) to be warped when projecting the SfM model onto a flat surface for creation of a 2D orthophoto mosaic.

Prior methods of accurately scaling photomosaics of paleoseismic trenches using SfM have relied on control points surveyed with either a total station or dGPS (Reitman et al., 2015) or by placing printed scale bars throughout the trench exposure (e.g., Delano et al., 2021). The total station and dGPS methods are time-consuming and require expensive instruments, and in the case of dGPS, may not produce the necessary accuracy in a forested or urban environment. The scale bar method, while cost-effective and quick for a single trench exposure, does not produce a model in a reference frame that can readily be combined with other exposures (critical for 3D trenching), nor are scale bars able to independently correct bowl effects.

The methods presented in this manuscript build on those of Reitman et al. (2015) by substituting the dGPS or total station for the more readily available, easy to use, and cheap iOS (or other) laser scanner. Our method quickly surveys dozens of control points without the



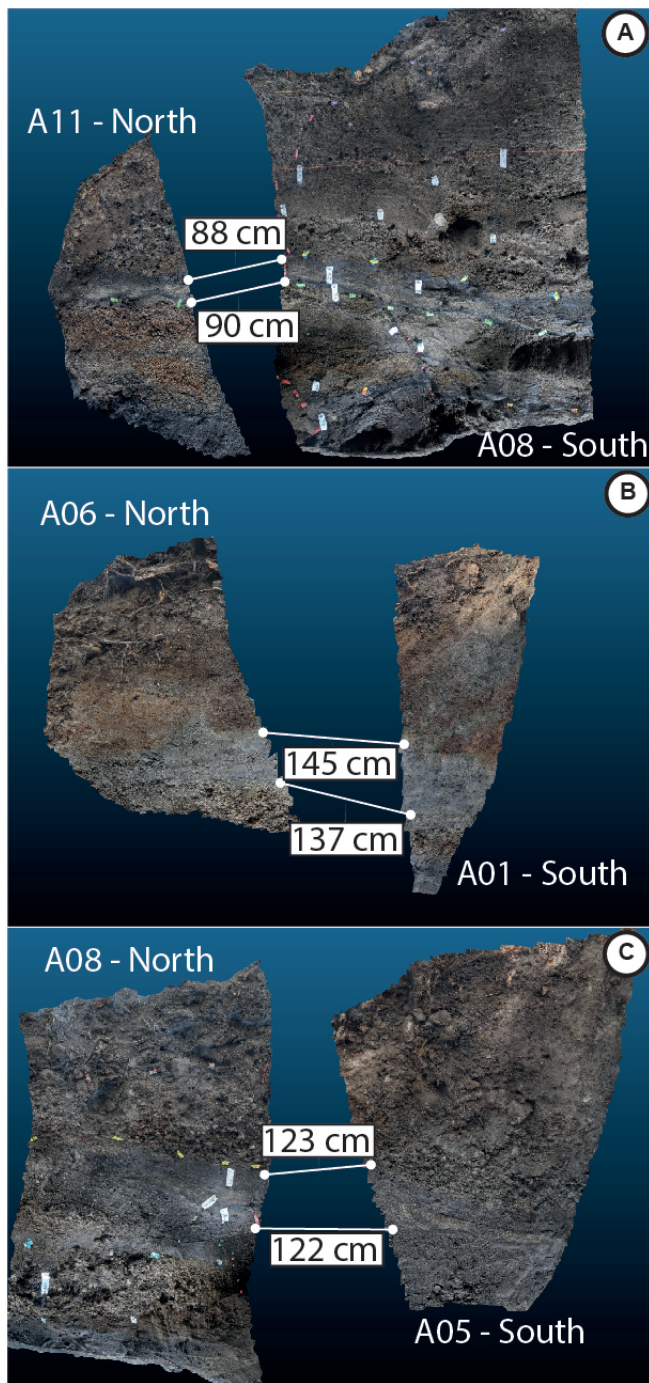


**Figure 7** Oblique 3D views showing manual offset estimation via trench slices that have been cut along the fault and are effectively ‘backslipped’ to find the best matching strata. Measurements indicated are the distances between the two matching contacts on opposite sides of the fault, which is an estimate for the displacement.

need for expensive and cumbersome equipment. The resulting iOS scans can be quickly field-verified on the collecting device and then imported and used to produce control points directly in SfM software (e.g. Agisoft Metashape). We also build on a method suggested by Bemis et al. (2014), of collocating 3D trench models into a single digital reference frame. This method places models of progressively excavated 3D paleoseismic trenches into a single 3D model, moving beyond more traditional 2D trench analysis.

Our results show that 3D paleoseismic trenching is greatly enhanced using these surveying methods and 3D software to constrain and model the geometry and orientations of a number of trench slices in a rapid, portable, and cost-effective way. Compared to a single trench, having multiple exposures allowed for the calculation of a robust single event fault displacement and increased confidence in a multiple-event interpretation. Visualization of the resulting 3D trench is greatly improved using modern 3D structural analysis software instead of more traditional pseudo-3D methods using 2D images. This method also more readily allows others to review the trench results in a high detail, realistic format.

## 6 Conclusions

Here we developed improved methods of 3D paleoseismic trench scanning, logging, and visualization. These cost-effective methods use an iOS laser scanner to establish control points between progressive 3D trenching excavations. Collocating these models into a single reference frame allows for improved visualization and more robust estimates of strike-slip fault displacement. The iOS scanner is useful not only for 3D trenches, but also for accurately scaling models of single trenches and for mitigating bowl effects. We used these methods to determine that a left-lateral offset of  $115 \pm 30$  cm occurred during a single earthquake after 8051 cal. ybp on the Dog Valley fault in northeast California. Based on the length of the fault and estimated offset it is inferred that this event may have had a magnitude of  $M_w 6.7 \pm 0.1$ . The penultimate earthquake on the Dog Valley fault occurred between 8491–8345 cal. ybp. While the broad range of ages allows that the Dog Valley fault may have contemporaneously ruptured with the Polaris fault, further investigation is required to determine if there is any possible triggering relationship with the conjugate & intersecting right-lateral Polaris fault.

## Acknowledgements

We are grateful for discussions in the field with C., D., & O. Madugo, T. Dawson, G. Seitz, J. Zachariassen, S. Wesnousky, J. Bormann, J. McNeil, K. Adams, and K. Knudsen, and advice from R. Arrowsmith in reconstructing the trench model. We are grateful to editor Randolph Williams, and reviews from Sean Bemis and one anonymous reviewer that greatly improved the manuscript. Thanks to R. Hutchinson and J. Cañas of Tahoe National Forest for assisting in permitting access. Research supported by U.S. Geological Survey (G20AP00055). Any use of trade, firm, or product names is for descriptive purposes only and does not imply endorsement by the U.S. Government. Ian Pierce is supported by the Leverhulme Trust project ‘EROICA’.

## Data and code availability

All data used in this study are publicly available and listed below.

OxCal v4.4.4 Bronk Ramsey (2021); r:5 Atmospheric data from Reimer et al (2020)

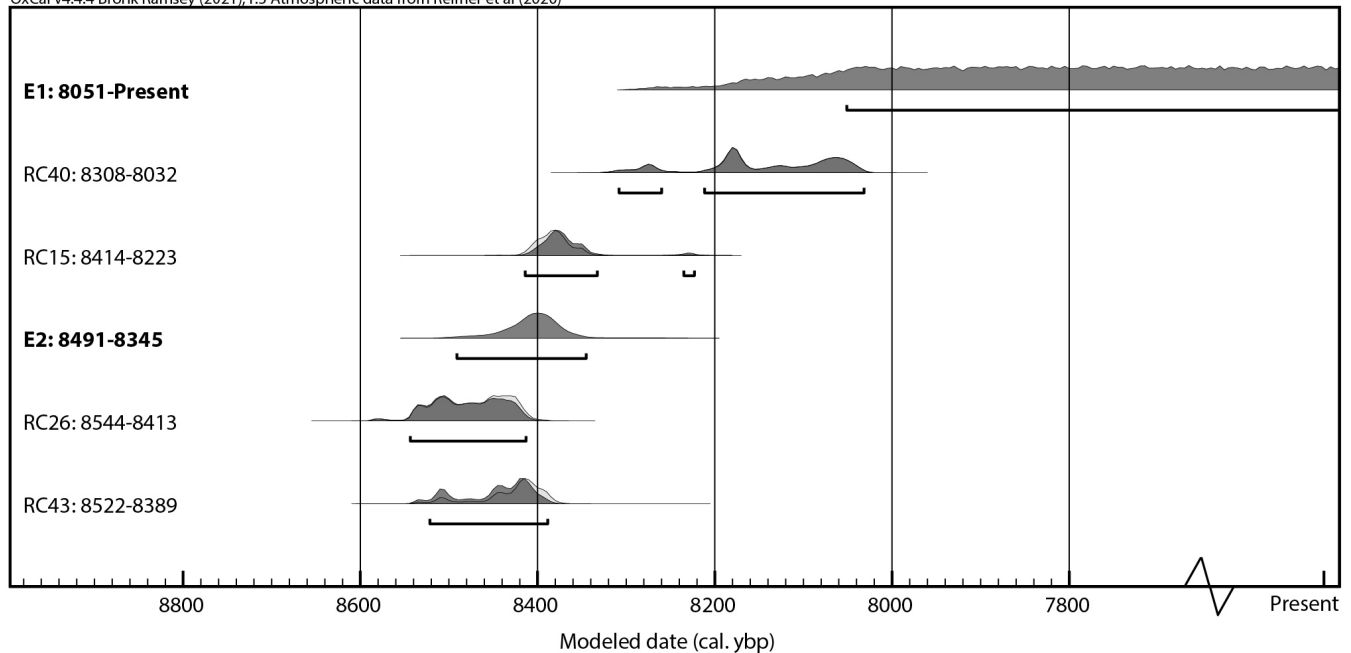


**Figure 8** OxCal sequence model of radiocarbon ages showing event horizons. Events E1 and E2 occurred after 8051 and from 8491-8345 cal. ybp, respectively.

Mapped traces from this study of the Dog Valley fault in shapefile format are available here: <https://doi.org/10.5281/zenodo.6986415>

Orthoimages of the trench walls are available here: <https://doi.org/10.5281/zenodo.6986465>

3D Surface textures of trench walls are available here: <https://doi.org/10.5281/zenodo.7341261>

OxCal sequence model code is listed in the supplementary material.

Airborne lidar data used in the study are freely available from opentopography.org: <https://doi.org/10.5069/G9V122Q1>

## Competing interests

The authors have no competing interests.

## References

- Agisoft LLC. Agisoft Metashape Professional, 2022.
- Barnhart, W., Lohman, R., and Mellors, R. Active accommodation of plate convergence in Southern Iran: Earthquake locations, triggered aseismic slip, and regional strain rates: SOUTHERN IRAN ACTIVE DEFORMATION. *Journal of Geophysical Research: Solid Earth*, 118(10):5699–5711, 2013. doi: 10.1002/jgrb.50380.
- Barnhart, W., Hayes, G., and Gold, R. The July 2019 Ridgecrest, California Earthquake Sequence: Kinematics of Slip and Stressing in Cross-Fault Ruptures. *Geophysical Research Letters*, 2019. doi: 10.1029/2019GL084741.
- Bemis, S., Mickelthwaite, S., Turner, D., James, M. R., Akciz, S., Thiele, S. T., and Bangash, H. A. Ground-based and UAV-Based photogrammetry: A multi-scale, high-resolution mapping tool for structural geology and paleoseismology. *Journal of Structural Geology*, 69:163–178, 2014. doi: 10.1016/j.jsg.2014.10.007.
- Bormann, J., Hammond, W., Kreemer, C., Blewitt, G., and Jha, S. A Synoptic Model of Fault Slip Rates in the Eastern California Shear Zone and Walker Lane from GPS Velocities for Seismic Hazard Studies. In *2013 Seismological Society of America Annual Meeting*, page 323, Salt Lake City, UT, 2013. Seismological Research Letters.
- Bormann, J., Hammond, W. C., Kreemer, C., and Blewitt, G. Accommodation of missing shear strain in the Central Walker Lane, western North America: Constraints from dense GPS measurements. *Earth and Planetary Science Letters*, 440:169–177, 2016. doi: 10.1016/j.epsl.2016.01.015.
- Bronk Ramsey, C. Radiocarbon Calibration and Analysis of Stratigraphy: The OxCal Program. *Radiocarbon*, 37(2):425–430, 1995. doi: 10.1017/S0033822200030903.
- Brothers, D., Kent, G., Driscoll, N., Smith, S., Karlin, R., Dingler, J., Harding, A., Seitz, G., and Babcock, J. New Constraints on Deformation, Slip Rate, and Timing of the Most Recent Earthquake on the West Tahoe-Dollar Point Fault, Lake Tahoe Basin, California. *Bulletin of the Seismological Society of America*, 99(2A):499–519, 2009. doi: 10.1785/0120080135.
- Delano, J., Briggs, R., DuRoss, C., and Gold, R. Quick and Dirty (and Accurate) 3D Paleoseismic Trench Models Using Coded Scale Bars. 2021. doi: 10.1785/0220200246.
- dePolo, C. and Ramelli, A. Preliminary report on surface fractures along the White Mountains fault zone associated with the July 1986 Chalfant Valley earthquake sequence. *Bulletin of the Seismological Society of America*, 77(1):290–296, 1987. doi: 10.1785/BSSA0770010290.
- Dingler, J., Kent, G., Driscoll, N., Babcock, J., Harding, A., Seitz, G., Karlin, B., and Goldman, C. A high-resolution seismic CHIRP investigation of active normal faulting across Lake Tahoe Basin, California-Nevada. *GSA Bulletin*, 121(7/8):1089–1107, 2009. doi: 10.1130/B26244.1.
- Gold, R., Briggs, R., Personius, S., Crone, A., Mahan, S., and Angster, S. Latest Quaternary paleoseismology and evidence of distributed dextral shear along the Mohawk Valley fault zone, northern Walker Lane, California: Paleoseismology Mohawk Valley fault zone. *Journal of Geophysical Research: Solid Earth*, 119(6):5014–5032, 2014. doi: 10.1002/2014JB010987.



- GPL Software. CloudCompare, 2022.
- Haddad, D., Akciz, S., Arrowsmith, J., Rhodes, D., Oldow, J., Zielke, O., Toke, N., A.G., H., Mauer, J., and Shilpakar, P. Applications of airborne and terrestrial laser scanning to paleoseismology. *Geosphere*, 8(4):771–786, 2012. doi: 10.1130/GES00701.1.
- Hall, N., Wright, R., and Clahan, K. Paleoseismic studies of the San Francisco Peninsula segment of the San Andreas Fault zone near Woodside, California. *Journal of Geophysical Research: Solid Earth*, 104(B10):23215–23236, 1999. doi: 10.1029/1999JB900157.
- Hammond, W., Blewitt, G., and Kreemer, C. Block modeling of crustal deformation of the northern Walker Lane and Basin and Range from GPS velocities. *Journal of Geophysical Research*, 116 (B4), 2011. doi: 10.1029/2010JB007817.
- Hanks, T. and Kanamori, H. A moment magnitude scale. *Journal of Geophysical Research: Solid Earth*, 84(B5):2348–2350, 1979. doi: 10.1029/JB084iB05p02348.
- Hatch-Ibarra, R., Abercrombie, R., Ruhl, C., Smith, K., HAMmond, W., and Pierce, I. The 2016 Nine Mile Ranch Earthquakes: Hazard and Tectonic Implications of Orthogonal Conjugate Faulting in the Walker Lane. *Bulletin of the Seismological Society of America*, 112, 2022. doi: 10.1785/0120210149.
- Hawkins, F., LaForge, R., and Hansen, R. Seismotectonic Study of the Truckee/Lake Tahoe Area Northeastern Sierra Nevada, California for Stampede, Prosser Creek, Boca, and Lake Tahoe Dams. *Seismotectonic Report*, (85-4):237, 1986.
- Hudnut, K., Seeber, L., and Pacheco, J. Cross-fault triggering in the November 1987 Superstition Hills Earthquake Sequence, southern California. *Geophysical Research Letters*, 16(2):199–202, 1989. doi: 10.1029/GL016i002p00199.
- Hunter, L., Howle, J., Rose, R., and Bawden, G. LiDAR-Assisted Identification of an Active Fault near Truckee, California. *Bulletin of the Seismological Society of America*, 101(3):1162–1181, 2011. doi: 10.1785/0120090261.
- Jaud, M., Passot, S., Allemand, P., Le Dantec, N., Grandjean, P., and Delacourt, C. Suggestions to Limit Geometric Distortions in the Reconstruction of Linear Coastal Landforms by SfM Photogrammetry with PhotoScan® and MicMac® for UAV Surveys with Restricted GCPs Pattern. *Drones*, 3(1):2, 2019. doi: 10.3390/drones3010002.
- Jones, L. and Hough, S. Analysis of broadband records from the. *Bulletin of the Seismological Society of America*, 85(3):688–704, 1995. doi: 10.1785/BSSA0850030688.
- Kent, G., J.M., B., Driscoll, N., Harding, A., Dingler, J., Seitz, G., Gardner, J., Mayer, L., Goldman, C., Heyvaert, A., Richards, R., Karlin, R., Morgna, C., Gayes, P., and Owen, L. 60 k.y. record of extension across the western boundary of the Basin and Range province: Estimate of slip rates from offset shoreline terraces and a catastrophic slide beneath Lake Tahoe. *Geology*, 33(5): 365–368, 2005. doi: 10.1130/G21230.1.
- Li, X., Huang, W., Pierce, I., S.J., A., and Wesnousky, S. Characterizing the Quaternary expression of active faulting along the Olinghouse, Carson, and Wabuska lineaments of the Walker Lane. *Geosphere*, 13(6):2119–2136, 2017. doi: 10.1130/GES01483.1.
- Luetzenburg, G., Kroon, A., and Bjørk, A. Evaluation of the Apple iPhone 12 Pro LiDAR for an Application in Geosciences. *Scientific Reports*, 11(1):22221, 2021. doi: 10.1038/s41598-021-01763-9.
- Marco, S., Rockwell, T., Heimann, A., Frieslander, U., and Agnon, A. Late Holocene activity of the Dead Sea Transform revealed in 3D palaeoseismic trenches on the Jordan Gorge segment. *Earth and Planetary Science Letters*, 234(1–2):189–205, 2005. doi: 10.1016/j.epsl.2005.01.017.
- McCalpin, J. *Paleoseismology*. Academic Press, 2nd edn edition, 2009.
- Melody, A., Whitney, B., and Slack, C. Late Pleistocene and Holocene Faulting in the Western Truckee Basin North of Truckee, California. *Bulletin of the Seismological Society of America*, 102(5):2219–2224, 2012. doi: 10.1785/0120110260.
- Olig, S., Sawyer, T., Wright, D., Terra, F., and Anderson, L. Preliminary seismic source characterization of faults near Stampede and Prosser Creek dams-Washoe Project and Boca dam-Truckee Storage Project, northern Sierra Nevada. 2005.
- OpenTopography. 2014 USFS Tahoe National Forest Lidar, 2017.
- Pierce, I., Wesnousky, S., and Owen, L. Terrestrial cosmogenic surface exposure dating of moraines at Lake Tahoe in the Sierra Nevada of California and slip rate estimate for the West Tahoe Fault. *Geomorphology*, 298:63–71, 2017. doi: 10.1016/j.geomorph.2017.09.030.
- Pierce, I., Wesnousky, S., Owen, L., Bormann, J., Li, X., and Caffee, M. Accommodation of Plate Motion in an Incipient Strike-Slip System: The Central Walker Lane. *Tectonics*, 40(2), 2021. doi: 10.1029/2019TC005612.
- Reed, T. *Spatial Correlation of Earthquakes with Two Known and Two Suspected Seismogenic Faults, North Tahoe-Truckee Area, California*. Master's Thesis. Baylor University, 2014.
- Reitman, N., Bennett, S., Gold, R., Briggs, R., and DuRoss, C. High-Resolution Trench Photomosaics from Image-Based Modeling: Workflow and Error Analysis. *Bulletin of the Seismological Society of America*, 105(5):2354–2366, 2015. doi: 10.1785/0120150041.
- Rezapour, M. and Mohsenpur, A. The 2010 Mw 6.5 Rigan, Iran, Earthquake Aftershock Sequence. *Bulletin of the Seismological Society of America*, 103(3):1793–1800, 2013. doi: 10.1785/0120120288.
- Rockwell, T., Ragona, D., Seitz, G., Langridge, R., Aksoy, M., Ucarus, G., Ferry, M., Meltzner, A., Klinger, Y., Meghraoui, M., Satir, D., Barka, A., and B., A. Palaeoseismology of the North Anatolian Fault near the Marmara Sea: implications for fault segmentation and seismic hazard. *Geological Society, London, Special Publications*, 316(1):31–54, 2009. doi: 10.1144/SP316.3.
- Ruhl, C., Abercrombie, R., Hatch, R., and Smith, K. Seismogenic Depth Variation across the Transtensional Northern Walker Lane. *Geophysics [preprint]*, 2020. doi: 10.1002/es-soar.10504612.1.
- Smith, K. and Priestley, K. Faulting in the 1986 Chalfant, California, Sequence: Local Tectonics and Earthquake Source Parameters. *Bulletin of the Seismological Society of America*, 90(4):813–831, 2000. doi: 10.1785/0119990129.
- Sylvester, A. and Raines, G. *Geology of the Independence Lake and Hobart Mills Quadrangles, Truckee, California*, 2013.
- U.S.G.S. U.S. Geological Survey Quaternary fault and fold database for the United States, 2020.
- Walker, R., Bergman, E., Szeliga, W., and Fielding, E. Insights into the 1968–1997 Dasht-e-Bayaz and Zirkuh earthquake sequences, eastern Iran, from calibrated relocations, InSAR and high-resolution satellite imagery: Dasht-e-Bayaz and Zirkuh earthquake sequences. *Geophysical Journal International*, 187 (3):1577–1603, 2011. doi: 10.1111/j.1365-246X.2011.05213.x.
- Walker, R., Bergman, E., Elliot, J., Fielding, E., Ghods, A.-R., Ghoraishi, M., Jackson, J., Nazari, H., Nemati, M., Oveisi, B., Talebia, M., and Walters, R. The 2010–2011 South Rigan (Baluchestan) earthquake sequence and its implications for distributed deformation and earthquake hazard in southeast Iran. *Geophysical Journal International*, 193(1):349–374, 2013. doi: 10.1093/gji/ggs109.
- Wesnousky, S. Active faulting in the Walker Lane. *Tectonics*, 24(3):

35, 2005. doi: 10.1029/2004TC001645.

Wesnousky, S. Displacement and Geometrical Characteristics of Earthquake Surface Ruptures: Issues and Implications for Seismic-Hazard Analysis and the Process of Earthquake Rupture. *Bulletin of the Seismological Society of America*, 98(4): 1609–1632, 2008. doi: 10.1785/0120070111.

Wesnousky, S., Bormann, J., Kreemer, C., Hammond, W., and Brune, J. Neotectonics, geodesy, and seismic hazard in the Northern Walker Lane of Western North America: Thirty kilometers of crustal shear and no strike-slip? *Earth and Planetary Science Letters*, 329–330:133–140, 2012. doi: 10.1016/j.epsl.2012.02.018.

The article *3D Paleoseismology of the Dog Valley Fault (California, USA) from iOS Lidar and Structure-from-Motion Photogrammetry* © 2023 by Ian K.D. Pierce is licensed under CC BY 4.0.